

On Abnormal Execution Timing of Conditional Jump Instructions

Annika Wilde
annika.wilde@rub.de
Ruhr University Bochum
Germany

Samira Briongos
samirabriongos@gmail.com
NEC Laboratories Europe
Germany

Claudio Soriente
csoriente@gmv.com
GMV Spain
Spain

Ghassan Karamé
ghassan@karamé.org
Ruhr University Bochum
Germany

Abstract

An extensive line of work on modern computing architectures has shown that the execution time of instructions can (i) depend on the operand of the instruction or (ii) be influenced by system optimizations, e.g., branch prediction and speculative execution paradigms.

In this paper, we systematically measure and analyze timing variabilities in conditional jump instructions that can be macro-fused with a preceding instruction, depending on their placement within the binary. Our measurements indicate that these timing variations stem from the μ op cache placement and the jump's offset in the L1 instruction cache of modern processors. We demonstrate that this behavior is consistent across multiple microarchitectures, including Skylake, Coffee Lake, and Kaby Lake, as well as various real-world implementations. We confirm the prevalence of this variability through extensive experiments on a large-scale set of popular binaries, including libraries from Ubuntu 24.04, Windows 10 Pro, and several open-source cryptographic libraries. We also show that one can easily avoid this timing variability by ensuring that macro-fusible instructions are 32-byte aligned—an approach initially suggested in 2019 by Intel in an overlooked short report. We quantify the performance impact of this approach across the cryptographic libraries, showing a speedup of 2.15% on average (and up to 10.54%) when avoiding the timing variability. As a by-product, we show that this variability can be exploited as a covert channel, achieving a maximum throughput of 16.14 Mbps.

1 Introduction

Software instructions exhibit unintended variations in their execution time that may affect a program's performance and security. For example, Großschädl *et al.* [14] and Andryscy *et al.* [5] demonstrated that the type of operand(s) influences the execution time of multiplications and floating-point operations on certain processors. Other works have uncovered and exploited time variations arising from cache memories [3, 23, 29], port contention [2], speculative execution [9, 21], and branch predictions [1]. Another line of work has explored timing fluctuations caused by the decode procedure in the processor's front-end. For example, Kim *et al.* [20] and Ren *et al.* [24] reverse engineer the μ op cache and show that cache contention results in measurable timing differences that can be exploited to exfiltrate information. Deng *et al.* [10] characterize and exploit diverging decode times of the available decode paths. Finally, Wang *et al.* [25] analyze stalls in the decoder and measure their security impact.

In this paper, we take a different approach and systematically analyze and measure the timing variations of conditional jump instructions due to instruction placement in the binary. In particular, our measurements show that the position of a conditional jump in the binary affects macro-op fusion and the caching of the

corresponding μ ops in the μ op cache, which in turn determines the instruction fetch time. We stress that such behavior (i) does not depend on the instruction operand (e.g., the jump target), (ii) is orthogonal to both branch prediction and speculative execution, and (iii) does not rely on cache contention.

We measure the prevalence of this timing variability by means of thorough experiments and show that up to 15.6% of all macro-fusible conditional jump instructions identified in our experiments are likely to be on a “slow path”—incurring additional cycles for execution. Among these conditional jumps that require additional cycles, our findings suggest that 10% of those result from failed macro-op fusion, while the remaining 90% are caused by a microcode update introduced by Intel, resulting in an increased number of fetches due to μ op cache misses (cf. Section 3). We demonstrate that this behavior is consistent across multiple microarchitectures, including Skylake, Coffee Lake, and Kaby Lake. Surprisingly, our measurements show that AMD architectures exhibit similar behavior, though driven by different factors; namely, we show that 7.8% of all jump instructions in AMD Zen 3 are likely to exhibit a slow path due to an increased number of micro-op cache fetches (cf. Section 4).

We validate our measurements with a large-scale study of 666 real-world libraries, comprising 320 from a fresh Ubuntu 24.04.2 installation, 323 from a fresh Windows 10 Pro 22H2 installation, and 23 open-source cryptographic libraries. Surprisingly, the empirical results of our static analysis show that 99.7% of the Ubuntu libraries, 87.0% of the Windows libraries, and all cryptographic libraries conform to the expected 16% rate of macro-fusible conditional jumps on the slow path (cf. Section 5). These findings suggest that there is additional room to speed up the execution time. Namely, practitioners can easily reduce the execution time of their code by ensuring that macro-fusible instructions do not span 32-byte boundaries—an approach initially suggested in 2019 by Intel in an overlooked short report [16]. We quantify the performance impact of this approach by applying it to the set of cryptographic libraries. Namely, our experimental results show that this countermeasure yields an average improvement of 2.15%—with gains of up to 10.5% in some open-source cryptographic libraries (cf. Section 6).

As a by-product, we note that these timing variabilities in conditional jumps can allow an adversary to distinguish which branches are being executed in software—even when all branches are balanced. We show, using empirical analysis, that an adversary can achieve a maximum throughput of up to 16.14 Mbps by exploiting such variabilities to create a cross-core covert channel between two processes (Section 7).

We are currently in the process of responsibly disclosing our findings to Ubuntu, Microsoft, and the developers of the analyzed cryptographic libraries. At the time of writing, both WolfSSL and Amazon s2n-tls have officially adopted our recommendations.

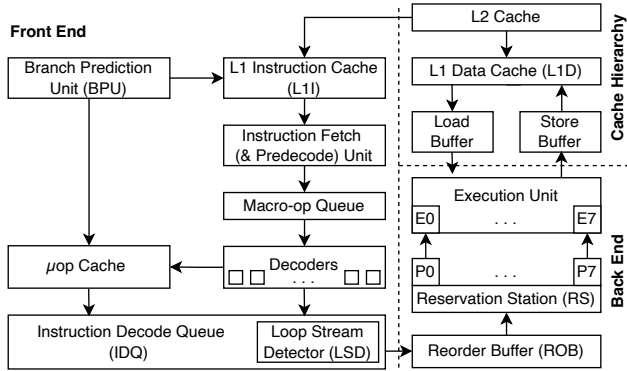


Figure 1: Overview of the x86 microarchitecture.

2 Background & Related Work

In this section, we provide an overview of the x86 microarchitecture and the organization of the μ op cache, and briefly discuss related work on timing variability in the x86 front-end.

2.1 x86 Microarchitecture

The x86 microarchitecture typically comprises three high-level components: the front-end, the back-end, and the memory subsystem. These components handle various tasks, such as fetching, decoding, executing instructions, and retrieving data. Figure 1 illustrates the critical elements of the x86 microarchitecture and their relationships.

Cache Hierarchy. Memory is organized in pages, typically of 4KB size. Given that access to the main memory incurs a high latency, modern processors feature three levels of cache: Last Level Cache (LLC), Level 2 Cache (L2), and Level 1 Cache (L1). The L1 cache has the least latency and is, in contrast to the other caches, divided into an instruction (L1I) and data cache (L1D). Recent x86 CPUs feature an additional micro-op cache (μ op cache), which stores the translation of instructions into micro-ops and has an even lower latency than the L1I cache (cf. Section 2.2).

Note that the L2 and L1D caches belong to the memory subsystem, whereas the L1I cache belongs to the front-end. Also, L1D is accessed by the back-end through the load and store buffers which accelerate the memory accesses.

The front-end. The x86 instruction set architecture (ISA) defines a set of complex instructions with varying instruction lengths. The front-end is responsible for fetching and decoding these “variable-length” instructions. Memory lines are loaded into the L1I cache from the L2 cache. Current x86 processors can fetch up to 64 bytes per cycle. The *instruction fetch unit* then fetches 16- or 32-byte-aligned blocks from the L1I cache. In Intel processors, the fetch unit includes a *pre-decoder* that marks the bounds of the variable-length instructions for subsequent processing. The pre-decoder outputs so-called *macro-ops*, which are stored in the *macro-op queue*. Note that the instruction fetch unit only forwards complete macro-ops. When an instruction crosses a fetch boundary, the unit waits until the following cycle, after the rest of the instruction bytes are fetched, before forwarding the complete macro-op.

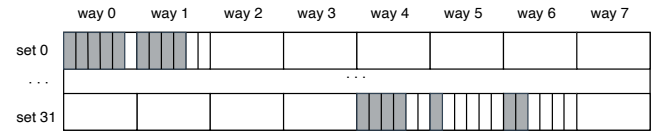


Figure 2: Overview of the micro-op cache of Intel’s Skylake microarchitecture. Gray fields represent used μ op slots, indicating that the cache holds valid μ ops ready to be streamed to the IDQ. White fields represent empty or skipped slots due to the cache’s placement policy or alignment restrictions.

The macro-op queue buffers macro-ops and optionally performs *macro-op fusion*, where specific logic, arithmetic, and compare instructions are fused with a subsequent jump instruction to a single macro-op performing both operations.

On the other hand, the decoding unit translates the macro-ops into *micro-ops* (μ ops). Unlike macro-ops, μ ops are fixed in length and exhibit reduced complexity, enabling more efficient processing within the microarchitecture. The number of decoders in the decoding unit and the amount of μ ops output per cycle vary among manufacturers and architectures. For instance, the decoding unit of Intel’s Skylake microarchitecture contains five decoders and outputs up to five μ ops per cycle. The decoded μ ops are stored in the *μ op cache* to bypass the decoding for previously decoded instructions. The *branch prediction unit* (BPU) tries to predict whether a branch will be taken and, consequently, determines the address of the next instruction. Based on this prediction, the BPU checks the corresponding address in the μ op cache. Hence, μ ops are either provided by the μ op cache (μ op cache hit) or by the decoder (μ op cache miss), with the μ op cache offering higher throughput.

Finally, the μ ops are stored in the *instruction decode queue* (IDQ), which buffers between the front-end and back-end to mitigate stalls. Front-end stalls can arise from BPU mispredictions, μ op cache misses that require refilling the decode pipeline, or L1I cache misses. Insufficient μ op delivery may empty the IDQ, causing stalls due to the lack of μ ops for dispatch. Conversely, back-end stalls arise when it temporarily exceeds its capacity to process μ ops, prompting the IDQ to pause delivery. In some processors, the IDQ incorporates a loop stream detector (LSD), which detects loops up to 70 μ ops and streams them directly.

The back-end. The back-end executes μ ops. Namely, it receives a stream of in-order μ ops from the IDQ and stores them in the *reorder buffer* (ROB). The ROB performs optimizations, such as register renaming, elimination of register-to-register moves, and zeroing idioms. These optimizations allow skipping the execution of certain μ ops or to parallelize them by breaking dependencies. The ROB then delivers the μ ops to the *reservation station* (RS), which schedules them to suitable ports for delivery to the respective execution units. Each execution unit serves a specific function, such as arithmetic computation. Some units are duplicated to increase throughput and enhance parallel processing capabilities. At execution time, sequential μ ops may be executed in parallel or even out-of-order if they are independent. The ROB then sequentially retires the μ ops in the correct order as received from the IDQ.

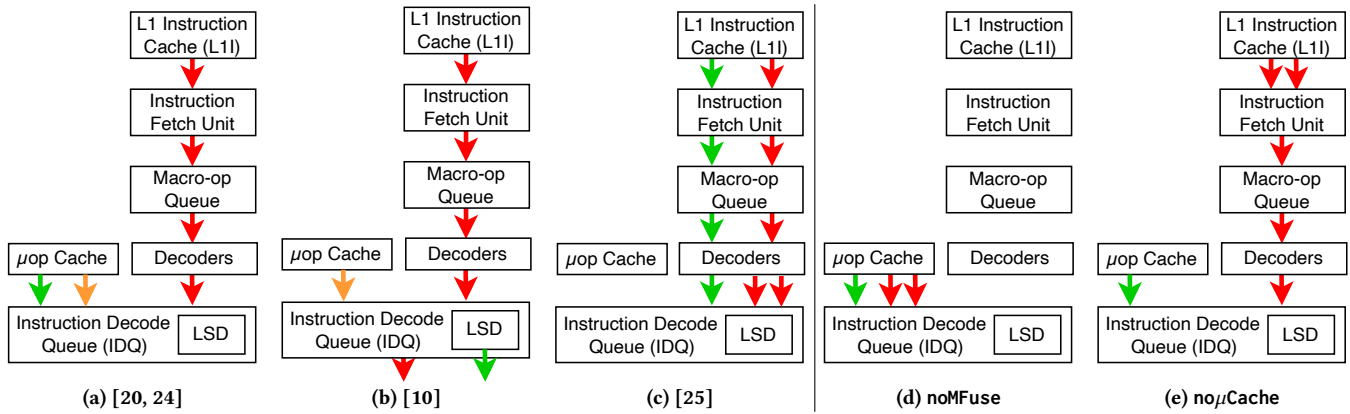


Figure 3: Overview of the x86 fetch paths in the front-end explored in related work (a-c) and this paper (d-e). Green arrows indicate the fast path, whereas red arrows denote the slow path. Two red arrows on the same path denote an additional cycle required for fetching. An orange arrow from the μ op cache represents a scenario in which the IDQ receives some μ ops from the μ op cache while others originate from the decoding pipeline, introducing delays for refilling the decoding pipeline.

2.2 Micro-op Cache

The micro-op cache buffers translated μ ops, allowing to bypass the decode pipeline (i.e., fetching, pre-decoding, and decoding) for recently decoded μ ops. The μ op cache is organized in cache sets and cache lines. Figure 2 illustrates the μ op cache of Intel’s Skylake architecture. Here, the μ op cache consists of 32 sets and eight ways, and can hold up to six μ ops per cache line (i.e., a specific set and way) [11]. The cache set is indexed by the bits 5–9 of the respective instruction. It differs from other cache levels in that the μ op cache has complex additional placement rules and does not buffer every μ op [24]. For instance, the μ op cache can only store μ ops of a 32-byte-aligned code region if the corresponding μ ops fit within three cache lines. Otherwise, the region will always be fetched from the decode pipeline. Additionally, μ ops derived from the same macro-op must be placed in the same cache line. Finally, an unconditional jump must always be the last μ op in a cache line, among other placement rules. Hence, a μ op cache line may have empty slots depending on these constraints, as illustrated in Figure 2. The μ op cache of AMD CPUs is organized similarly with deviating sizes [20].

The μ op cache can stream μ ops corresponding to up to 64B per cycle in some processors, significantly increasing the throughput. The decode pipeline is inactive while μ ops are streamed from the μ op cache. If a μ op cache miss occurs, the front-end switches to decode the pipeline, incurring a delay to refill the pipeline.

2.3 Related Work

Previous research has highlighted the time variations due to the different paths that a code block can take to reach the back-end. Ren *et al.* [24] and Kim *et al.* [20] focus on reverse engineering the μ op cache and leverage these insights to create covert- and side-channels based on μ op cache contention. Deng *et al.* [10] explore the timing variations due to the different paths a block of code can take in the decode pipeline; they show a covert-channel where the sender forces specific decode paths to transmit information to a receiver. Finally, Wang *et al.* [25] explore stalls in the decoding unit triggered by specific combinations of fusible macro-ops. Decoders

have a limited capacity for macro-op fusion per cycle, and once this limit is reached, decoding halts. This results in an additional cycle to process the same number of instructions, leading to a measurable delay.

Figure 3(a-c) offers a detailed overview of the front-end timing variations studied in previous research. We point out that none of these works [10, 20, 24, 25] covers the front-end timing abnormalities that we discuss in Section 3 or measures the performance impact of the timing variations in real-world binaries. Furthermore, the covert-channels introduced in [10, 20, 24, 25] rely on either cache contention or stalls in the front-end decoder; in contrast, the covert-channel that we describe in Section 7 does not require any contention on shared resources between the sender and the receiver.

3 Abnormal Timing in Conditional Jumps

As mentioned in Section 2.3, execution-time variability due to the front-end of x86 microarchitectures has been thoroughly analyzed by [10, 20, 24, 25].

In this paper, we systematically measure and analyze two additional behaviors of x86 front-ends that incur timing differences in conditional jumps based on the instruction placement within the binary.

3.1 noMFuse: Impact of Misalignment on Macro-Op Fusion

Modern x86 microarchitectures optimize performance by fusing certain logic, arithmetic, and comparison instructions with a subsequent jump instruction into a single macro-op, which is then translated into a single μ op. This optimization reduces the load on the μ op cache and downstream microarchitectural components. However, we observe that specific placement of jump instructions can prevent macro-op fusion [17]. In such cases, the two instructions remain unfused and are translated into separate μ ops. Additionally, this placement causes the resulting μ ops to be stored in distinct μ op cache sets. Since the IDQ cannot fetch μ ops from

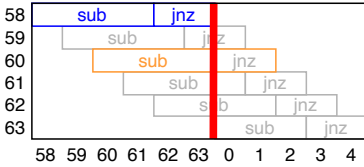


Figure 4: Different placement of a macro-fusible sub and jnz instruction within a 64-byte block. The 32/64B-aligned boundary is marked in red. Those instructions not crossing this boundary are marked in blue, those preventing macro-op fusion (noMFuse) are highlighted in orange, and the other ones (no/Cache) are marked in gray.

two different μ op cache sets within the same cycle, two cycles are required to fetch both instructions (cf. Figure 3d). In contrast, when the instructions are macro-fused and translated into a single μ op, they can be fetched in a single cycle. This difference introduces a one-cycle timing variation, depending on the placement of the fusible instruction pair.

We identify three different types of instruction placement that influence fetching. Figure 4 illustrates these placement scenarios using a four-byte sub instruction followed by a two-byte jnz instruction. In the first case, highlighted in blue, both instructions are located within the same 32-byte block, ensuring that they are consistently macro-fused and can be fetched within a single cycle from either the decode pipeline or the μ op cache. However, when the instruction pair spans a 32-byte boundary, an additional cycle is required for fetching, primarily due to delays in the instruction fetch unit. A special case arises when the instructions sub and jnz are placed in separate 64-byte blocks (highlighted in orange). This specific placement prevents macro-op fusion, as we further investigate in this section. Based on this analysis, a jump instruction encounters this special case with a probability of $\frac{1}{64} = 1.56\%$; that is, only one out of the 64 possible jump alignments within a 64-byte cache line positions the jump precisely at the boundary. In this scenario, the preceding fusible instruction lacks sufficient space within the same cache line, thereby preventing macro-op fusion.

In what follows, we additionally measure the impact of macro-op fusion on the front-end (which we dub noMFuse) and analyze the timing exhibited by an exemplary loop (cf. Figure 5). Notice that the loop contains only two instructions: a sub instruction, decrementing the loop counter at each iteration (cf. line 13), and a jnz instruction, jumping back to the beginning of the loop if the counter is not zero (cf. line 14).

Setup. Unless stated otherwise, we execute all experiments on an Intel Xeon E-2286G CPU, which is based on the Coffee Lake microarchitecture, with 128GB RAM running Ubuntu 20.04 LTS. We reserve a physical core for the experiments using the `isolcpus` option at boot-up and disable hyperthreading, ensuring that neither hyperthreading nor other processes interfere with the experiments. We then enforce the execution of the experiments on the reserved core. In addition, we fix the CPU frequency to disable dynamic voltage and frequency scaling (DVFS). Last but not least, we flush all caches before starting each measurement. We also repeat the

```

1  .rept B
2  NOP # shift the loop position
3  .endr
4
5  lfence
6  call PAPI_read
7  lfence
8  rdtsc
9  lfence
10
11 mov rcx,0xc8
12 loop:
13     sub rcx, 1
14     jnz loop
15
16 lfence
17 rdtsc
18 lfence
19 call PAPI_read

```

Figure 5: Example of a loop that decrements a counter by one and jumps to the loop start if the counter is not zero. The loop is instrumented to measure the execution time and different hardware events. The position of the loop in the binary is changed by modifying the number B of NOP instructions.

experiments over multiple days after restarting the machine to ensure that a primed machine state does not influence the results.

Our experiments are based on the code snippet in Figure 5. Lines 1-3 implement an optional padding with NOP instructions to change the location of the loop in the compiled binary. We repeat the padding instruction B times to achieve a shift by B bytes. We vary B between zero and 63 to encompass all possible offsets within an L1I cache line. We measure the timing difference with the `rdtsc` instruction in lines 8 and 17, which returns the number of cycles since the last restart. The counter provides an accuracy of 1-3 cycles on Intel CPUs. We place fences before and after the `rdtsc` instruction to ensure that the previous code (e.g., the varying shift) does not interfere with our measurements. We also monitor selected hardware performance counters (HPCs) to examine the behavior of the respective micro-architectural components in lines 6 and 19. Table 8 summarizes the observed HPCs and the specific events they capture. Line 11 initializes a counter to determine the number of consecutive jump instructions executed during a single measurement. We set the counter to 200, ensuring that the loop executes 200 jumps (to achieve a stable output execution time for profiling). Line 13 then decrements the counter and sets the flags for the jump instruction in line 14. All data points are averaged over 1000 independent runs.

Detailed findings. The overall timing variability of the code in Figure 5 is depicted in Figure 6. Here, we define the offset as the six least significant bits of the loop address. Our initial observation is based on execution timing: when placed in offsets 27-31 or 59-63, the execution time increases by approximately 200 cycles compared to other offsets. This corresponds to an overhead of approximately one cycle per iteration, averaged over 200 loop iterations.

Moreover, we observe that the x86 microarchitecture processes loop instructions differently when placed at offset 60. Table 1 presents our measurement results for selected offsets and HPCs to validate this observation. For the sake of simplicity, we discuss our results based on these representative offsets and refer the reader to Figure 8(a-d) for a comprehensive view of all 64 offsets. The first row of the table shows the execution time for offsets 0, 32, and 60.

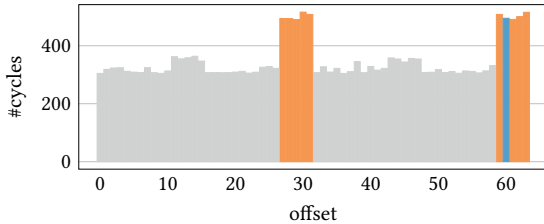


Figure 6: Execution time of the loop in Figure 5 for varying offsets. Offsets corresponding to noMFuse are highlighted in blue, and those corresponding to no μ Cache are highlighted in orange. All other offsets are represented in grey. Each data point is averaged over 1000 independent runs.

Table 1: Events for a selected subset of offsets and HPCs relevant for noMFuse in the Coffee Lake microarchitecture.

HPC	event	offset		
		0	32	60
rdtsc	execution cycles	305	307	495
BACLEAR.S.ANY	branch mispredictions	29	29	28
INSTRUCTIONS	executed instructions	651	651	651
UOPS_ISSUED.ALL	issued μ ops	611	616	780

Notably, offset 60 exhibits an increased execution time of approximately 190 cycles compared to offsets 0 and 32, confirming our initial observation. Note that this increased execution time is independent of branch prediction, as evidenced by the BACLEAR.S.ANY HPC, which reports a constant number of front-end re-steers. Furthermore, this behavior is not due to a difference in the number of executed instructions (see the third row of Table 1).

Instead, as shown in the fourth row, the primary cause of this discrepancy is a higher number of μ ops issued. Specifically, the number of issued μ ops for offsets 0 and 32 remains around 600, whereas for offset 60, the count approaches 800. This discrepancy arises due to an architectural feature of macro-op fusion in x86 processors, where the sub and jnz instructions can be fused to a single macro-op by the macro-op queue. The instruction decoders then translate this macro-fused instruction into a single μ op [25], which occupies a single slot in the μ op cache. However, Intel's x86 processors impose a restriction on macro-op fusion: if two fusible macro-ops are entirely located in different L1I cache lines, fusion does not occur [17]. Specifically, fusion is prevented if the jump instruction is 64B aligned. In our example, this happens when the loop is placed at offset 60. In this case, the two resulting μ ops are placed in separate 32B aligned code blocks, causing them to be stored in separate sets within the μ op cache. Since two sets cannot be accessed simultaneously, an additional cycle is required to fetch the two μ ops compared to the single μ op generated through macro-op fusion. Thus, the increased execution time that we measure at offset 60 is a direct consequence of failed macro-op fusion due to L1I cache alignment constraints.

3.2 no μ Cache: Impact of Misalignment on μ op-Caching

In Section 3.1, we discussed how instruction misalignment can prevent macro-op fusion in the front-end of modern x86 processors. We now examine a distinct effect of instruction misalignment that is caused by a microcode update issued by Intel for Skylake and later processors. We refer to this behavior as no μ Cache. Specifically, we observe that misaligning jump instructions and their predecessor can increase fetch and decode time in the front-end when the corresponding μ ops are not present in the μ op cache. In 2019, Intel released a microcode update to mitigate erratum SKX102, commonly referred to as the jump conditional code (JCC) erratum. This erratum can produce unpredictable behavior on certain Intel processors under specific microarchitectural conditions that involve jump instructions crossing 64-byte boundaries. In a short report, Intel states that the microcode update prevents jump instructions that cross or terminate on 32-byte boundaries from being retained in the μ op cache on the affected processors [16, Sec. 2.1 lines 1-3]. In such cases, the instruction fetch unit must retrieve the instructions from the L1I cache, fetching 16 bytes per cycle [24]. If the instructions are misaligned, the fetch unit must retrieve two blocks instead of one (cf. Figure 3e). However, the macro-op queue can only fuse the instructions once both are available. We observe that the macro-op queue waits an additional cycle to retrieve both instructions before attempting macro-op fusion. This introduces a timing variability of one cycle, depending on the placement of the jump instruction and its predecessor. Assuming that most jump instruction lengths range from 2-7 bytes and that the preceding fusible instructions are 3-5 bytes long,¹ the total length of a fusible instruction pair falls within five and 12 bytes, allowing for anywhere between four and 11 alignments to cross the 32-byte boundary. Based on this distribution, and excluding the alignment causing noMFuse, the likelihood of a fusible instruction pair encountering such alignment is lower-bounded by $\frac{7}{64} = 10.93\%$ and upper-bounded by $\frac{21}{64} = 32.81\%$. Our code in Figure 5 mimics this distribution by selecting a four-byte preceding instruction, which aligns with the observed average, followed by a standard two-byte conditional jump.

To validate this observation, we now analyze the timing behavior of the exemplary loop in Figure 5 using the same experimental setup detailed in Section 3.1. In the following, we present and discuss our findings.

Detailed findings. We witness an increased fetch time in the front-end for offsets 27-31, 59, and 61-63 when misaligning two macro-fusible instructions. Table 2 highlights the experimental results for selected offsets and HPCs to validate this observation. The execution time measurements in the first row of the table indicate that offset 31 exhibits an increased execution time of approximately 200 cycles compared to offsets 0 and 26, indicating that they undergo a different treatment by the microarchitecture.

As shown in the second row of Table 2, this timing discrepancy is caused by a stall in the IDQ, which serves as a μ op buffer between the front-end and the back-end. Specifically, the number of cycles where the IDQ does not deliver any μ ops to the back-end remains around 280 for offsets 0 and 26, whereas for offset 31, the HPC

¹We obtained these estimates from our analysis of 320 Ubuntu 24.04.2 default libraries (cf. Section 5).

Table 2: Events for a selected subset of offsets and HPCs relevant for no μ Cache in the Coffee Lake microarchitecture.

HPC	event	offset		
		0	26	31
rdtsc	execution cycles	305	322	508
IDQ_UOPS_NOT_DELIVERED.CYCLES_0_UOPS_DELIV_CORE	IDQ stall cycles	281	274	467
FRONTEND_RETIRE.DSB_MISS	μ op cache misses	74	230	230

reports 467 stalled cycles. Note that the hardware performance counter IDQ_UOPS_NOT_DELIVERED.CYCLES_0_UOPS_DELIV_CORE only counts IDQ stall cycles that are not caused by the back-end, confirming that these stalls originate in the front-end rather than in the back-end. The third row of the table presents measurements for the FRONTEND_RETIRE.DSB_MISS HPC, which counts the number of instructions experiencing μ op cache misses (i.e., instructions fetched via the decode pipeline rather than the μ op cache). We observe an increased number of μ op cache misses for offsets 26 and 31 compared to offset 0. This indicates that for offsets 26 and 31, loop instructions are fetched from the decode pipeline, whereas for offset 0, they are served directly from the μ op cache.

Recall that our experiments use a processor based on the Coffee Lake microarchitecture, where the instruction fetch unit retrieves one 16-byte aligned code block per cycle. Figure 4 illustrates the alignment of the two instructions in the loop for offsets 26-31. Notably, these offsets correspond to alignments for fusible instructions that are excluded from μ op cache residency by Intel’s microcode update [16, see Fig. 1, Examples 4-7] and therefore must be fetched via the decode pipeline. At offset 26, we note that the two instructions do not cross the 16-byte aligned boundary. Thus, the entire loop can be fetched in a single cycle, explaining the faster execution despite increased μ op cache misses. At offset 31, however, one of the instructions crosses the boundary, so they no longer fit within the same 16B fetch window.

Figure 7 illustrates how this leads to additional fetch delays in the decode pipeline. In the first scenario (top row), the sub and jnz instructions are placed within a single 16B block. The instruction fetch unit retrieves both instructions in a single cycle, delivering them together to the macro-op queue for fusion. The decoder then processes the fused instruction without additional delay. In contrast, in the second scenario (second and third row), the sub instruction is split across two blocks. In this case, the instruction fetch unit cannot deliver the incomplete instruction to the macro-op queue within the same cycle. Instead, the fetch unit must wait for the subsequent block, delaying macro-op fusion by one cycle. This additional fetch cycle causes a one-cycle delay in instruction execution. This scenario occurs for nine out of 64 offsets, i.e., with a probability of $\frac{9}{64} \leq 14.06\% \leq \frac{21}{64}$, well within the ranges obtained above.

A comprehensive view of our measurements for all 64 offsets is presented in Figure 8(a-d). Here, we highlight the offsets that prevent macro-op fusion (cf. Section 3.1) in blue, while those that increase the instruction fetch delay in the front-end (cf. Section 3.2) are marked in orange.

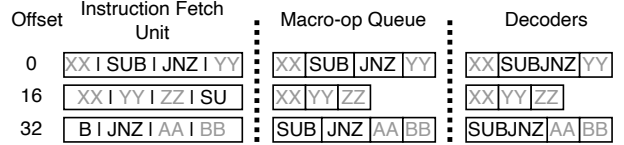


Figure 7: Overview of the decode pipeline for different placements of two fusible instructions. In the upper case, the instructions can be fetched without delay, whereas the lower case incurs a one-cycle delay for fetching the remainder of the sub instruction.

4 Impacted Architectures

Our analysis in Section 3 focuses on a specific processor, namely the Intel Xeon E-2286G CPU, which implements Intel’s Coffee Lake microarchitecture. We now examine the reproducibility of our findings across different processors and analyze the impact of the microarchitecture. Specifically, we performed the measurements described in Section 3.1 on eight different processors spanning seven distinct microarchitectures. Our experiments primarily consisted of profiling the execution time and logging HPC events for a sub-jnz loop with 200 iterations (cf. Figure 5). The last two rows in Figure 8 present an overview of the timing measurements, while Table 3 summarizes the HPC data for selected offsets discussed in our analysis in Section 3. Notice that variations in the naming of HPCs stem from slight naming variances on different architectures. Based on our findings, we classify the observed behavior into three distinct categories of reproducibility, detailed in the following sections.

4.1 Skylake, Coffee Lake, and Kaby Lake (R)

We start by examining the processors that exhibit timing behavior consistent with the Intel Xeon E-2286G CPU used in our primary experiments. Specifically, Figures 8e to 8i show that the Intel Xeon E-2286G, Xeon E-2176G, Core i7-8550U, Core i5-8350U, and Core i7-6300U CPUs all show similar timing variations. To validate that these variations come from noMFuse and no μ Cache effects, we analyzed the HPC data, as summarized in Table 3.

All examined CPUs show an increase of approximately 200 μ ops at offset 60 due to the lack of macro-op fusion for this offset (cf. Section 3.1). Moreover, at offsets 26 and 31, we observe an increase of approximately 180 μ op cache misses, while only offset 31 results in IDQ stalls caused by increased instruction fetch latency (cf. Section 3.2). Measured differences in execution cycles across these processors are primarily due to variations in their operating frequencies, as each CPU was tested at its respective base frequency.

These processors implement one of three closely related microarchitectures: Skylake, Coffee Lake, and Kaby Lake. Notably, Kaby Lake and Coffee Lake are distinct successors of Skylake but do not introduce significant front-end modifications. All three microarchitectures are affected by the Intel microcode update that modifies the μ op cache behavior [16]. Moreover, this microcode update affects several additional CPUs based on Amber Lake, Cascade Lake, Comet Lake, and Whiskey Lake. While we do not have access to these specific processors for testing, we expect that these microarchitectures are equally subject to noMFuse and no μ Cache.

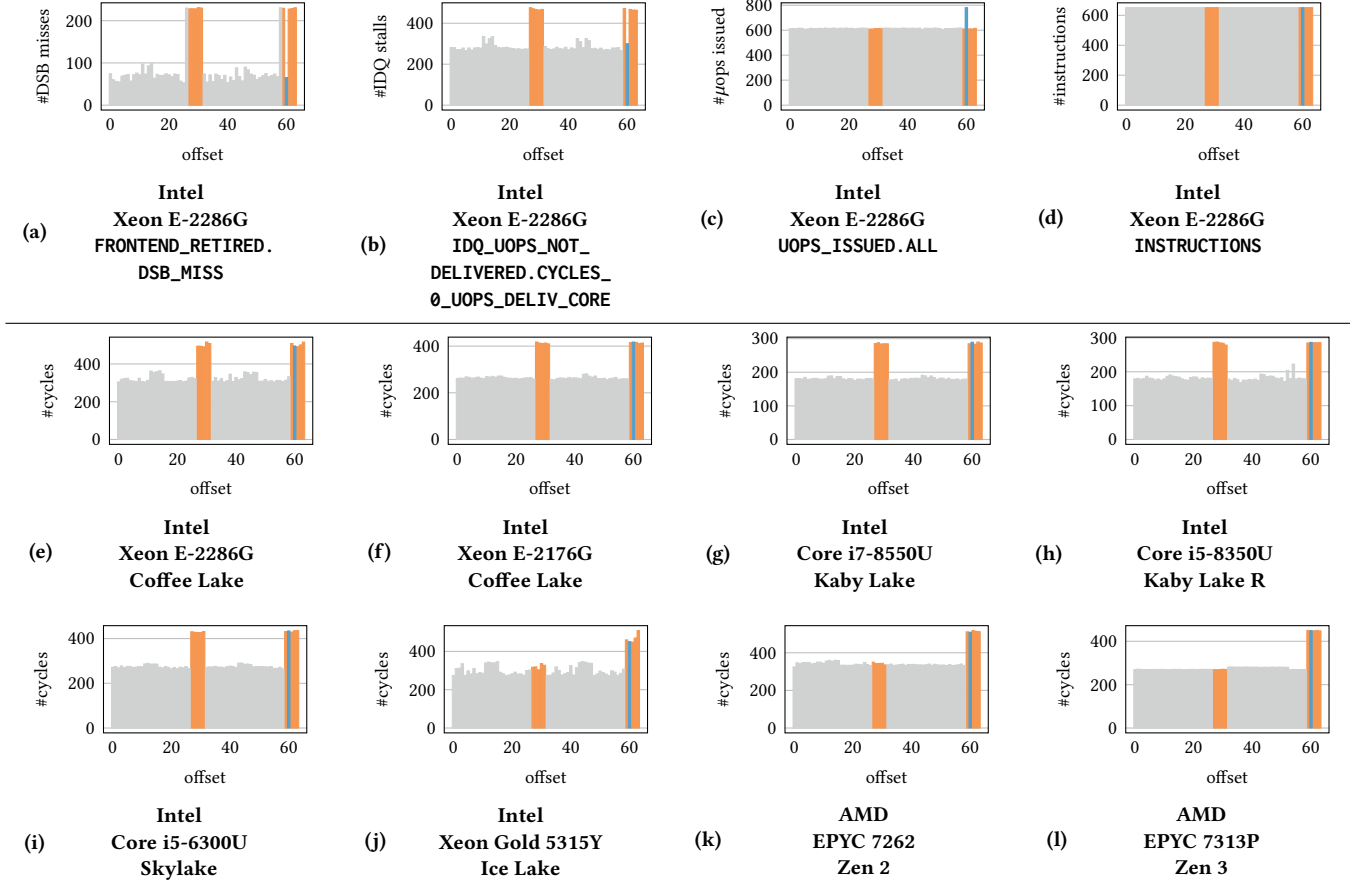


Figure 8: Results for various HPCs and x86 microarchitectures. The top row reports HPC measurements from a Coffee Lake-based CPU. The middle and bottom rows display execution time across multiple x86 processors and microarchitectures. Offsets corresponding to noMFuse are highlighted in blue, and those corresponding to no μ Cache are highlighted in orange. All other offsets are represented in grey. Each data point is an average over 1000 independent runs.

Note that the LSD, which caches small loops directly within the IDQ, was disabled by a microcode update on the Skylake, Coffee Lake, and Kaby Lake processors we analyzed, due to erratum SKL150 [22]. However, the LSD remains active on Amber Lake, Cascade Lake, Comet Lake, and Whiskey Lake processors. Since the LSD bypasses both the μ op cache (relevant to noMFuse) and the decode pipeline (relevant to no μ Cache), its use can mitigate the timing effects we observe. Nonetheless, we expect the LSD to only partially reduce the impact, as it does not cover all loops.

4.2 Ice Lake

We now analyze another Intel microarchitecture, namely Ice Lake. This architecture is particularly interesting because it is not listed among the affected microarchitectures in [16]. At first glance, the timing behavior of the profiled Xeon Gold 5315Y CPU appears similar to the patterns observed in Section 4.1. Specifically, we measure an additional 200 cycles in the execution time for offsets 59 to 63. However, a detailed examination of the corresponding HPC measurements in Table 3 reveals partially deviating root causes.

We find that approximately 140 additional μ ops are issued at offset 60, aligning with our observations from Section 3.1 and confirming that noMFuse remains effective on this architecture. When considering no μ Cache, although we witness an additional 200 IDQ stalls at offsets 59 and 61-63, our measurements suggest that these do not result from an increased number of μ op cache misses.

Note that processors based on the Ice Lake microarchitecture were introduced in 2021—two years after the publication of [16]. We hypothesize that Ice Lake (and subsequent microarchitectures) addresses the abnormality arising from the microcode update at a hardware level, such that the alignment previously associated with no μ Cache no longer prevents the corresponding μ ops from being cached in the μ op cache; however, the IDQ stalls remain as an artifact. The example of Ice Lake highlights that the observed timing variabilities are highly sensitive to the microarchitectural specifics of the front-end, suggesting that other front-end changes, such as a modified fetch window size in the Lion Cove micro-architecture, also influence how noMFuse and no μ Cache manifest. Consequently, individual inspection of each architecture is required to verify the manifestation of these issues.

Table 3: Number of events recorded for a selected subset of offsets and HPCs relevant to noMFuse and no μ Cache across various Intel and AMD processors. Values that are significantly higher at a specific offset compared to other offsets are highlighted in bold.

		Finding Offset	noMFuse		no μ Cache			
			0	32	60	26		
Intel	Coffee Lake	Xeon E-2286G	rdtsc	305	307	495	322	508
		UOPS_ISSUED.ALL		611	616	780	615	612
	Xeon E-2176G	FRONTEND_RETIRE.DSB_MISS		74	74	65	230	230
		IDQ_UOPS_NOT_DELIVERED.		281	286	300	274	467
		CYCLE_0_UOPS_DELIV_CORE						
Intel	Kaby Lake	i7-8350U	rdtsc	261	257	417	259	410
		UOPS_ISSUED.ALL		684	682	872	684	683
	i7-8350U	FRONTEND_RETIRE.DSB_MISS		47	50	46	229	230
		IDQ_UOPS_NOT_DELIVERED.		335	269	260	257	439
		CYCLE_0_UOPS_DELIV_CORE						
Intel	Kaby Lake R	i5-8350U	rdtsc	181	177	289	180	284
		UOPS_ISSUED.ALL		730	738	919	728	728
	i5-8350U	FRONTEND_RETIRE.DSB_MISS		50	48	49	231	232
		IDQ_UOPS_NOT_DELIVERED.		290	321	314	383	606
		CYCLE_0_UOPS_DELIV_CORE						

4.3 The Case of AMD

We now present a set of experiments to verify the occurrence of noMFuse on AMD’s Zen 2 and Zen 3 microarchitectures. We note that no μ Cache, which is a result of an Intel-specific microupdate [16], does not apply to AMD.

As shown in Figures 8k and 8l, the profiled EPYC 7262 and EPYC 7313P processors exhibit execution time patterns similar to those observed in Intel microarchitectures. Specifically, we observe an additional 180-200 cycle delay for offsets 59 to 63. Note that, in Zen 2, (i) this behavior is independent of the number of fused instructions (the RETIRED_FUSED_INSTRUCTIONS HPC consistently reports only 17 fused instructions across all offsets, aligning with the fact that Zen 2 exclusively fuses conditional jumps with test and cmp instructions [11].), and (ii) the number of μ ops dispatched from the μ op cache remains constant, confirming that all μ ops are retrieved from the μ op cache. However, loops with ≤ 5 instructions confined to 64B blocks can take a fast path, executing in one cycle per iteration (offsets 0-58), whereas crossing the boundary (offsets 59-63) adds a one-cycle penalty, since only one taken branch is executed every two cycles [11]. This effect mimics the behavior of noMFuse in x86 architectures.

In contrast, Zen 3 expands the set of fusible instructions such that we observe macro-op fusion for all offsets. That is, the sub and jnz are macro-fused and translated into a single μ op, occupying only one slot in a single μ op cache set. However, the OP_CACHE_HIT_MISS.OC_HIT HPC records approximately 200 additional hits in the μ op cache for offsets 60 and 63, suggesting that Zen 3 still accesses two distinct μ op cache sets. This introduces an additional cycle delay, mimicking the impact of noMFuse.

		Finding Offset	noMFuse		no μ Cache			
			0	32	60	26		
Intel	Skylake	i5-6300U	rdtsc	272	271	434	266	431
		UOPS_ISSUED.ALL		754	753	936	754	750
	Ice Lake	FRONTEND_RETIRE.DSB_MISS		53	54	52	230	231
		IDQ_UOPS_NOT_DELIVERED.		322	316	340	314	503
		CYCLE_0_UOPS_DELIV_CORE						
AMD	Zen 2	EPYC 7262	rdtsc	274	275	451	307	509
		RETIRED_FUSED_INSTRUCTIONS		600	611	742	606	601
	Zen 3	UOPS_DISPATCHED_FROM_DECODER.		35	34	70	39	51
		OPCACHE_DISPATCHED		182	183	210	199	397
		UOPS_QUEUE_EMPTY						
AMD	Zen 3	EPYC 7313P	rdtsc	325	336	508	332	512
		RETIRED_FUSED_INSTRUCTIONS		17	17	17	16	17
	Zen 3	OP_CACHE_HIT_MISS.OC_HIT		783	790	756	746	760
		UOPS_QUEUE_EMPTY		182	182	176	203	381

5 Abnormal Conditional Jumps in the Wild

To understand the real-world implications of our findings, we assess the prevalence of noMFuse and no μ Cache in 666 real-world binaries, ranging from popular cryptographic libraries to those shipped with current operating systems.

5.1 Methodology

To cover a wide range of real-world applications, we analyzed the binaries of libraries shipped with recent versions of two widely used operating systems: Ubuntu 24.04.2 and Windows 10 Pro 22H2. More specifically, we analyzed all the shared libraries installed per default on a fresh Ubuntu 24.04.2 installation. Moreover, we installed and analyzed the apt package build-essential, which includes a set of basic development tools, such as gcc and make. We retrieved the binaries of these libraries by executing the `/sbin/ldconfig -p` command, yielding 320 results. Similarly, we analyzed all the shared libraries installed per default on a fresh Windows 10 Pro 22H2 installation. Here, we retrieved the binaries of these libraries using a python script that extracts all DLL files in the “C:\Program Files (x86)” folder, yielding 323 results.

Besides analyzing the 320 libraries in Ubuntu 24.04.2 and the 323 libraries in Windows 10 Pro 22H2, we also analyzed a set of 23 cryptographic libraries (resulting in a total of 666 libraries), which are typically highly optimized for performance and security. Our selected cryptographic libraries are taken from [18]—which is, at the time of writing, one of the most extensive analyses of constant time behavior in cryptographic libraries. We focused our analysis on open-source libraries for the x86 microarchitecture and excluded

First instruction	Fusible conditional jumps
cmp	jz, jc, jb, ja, jl, jg, je
add	jz, jc, jb, ja, jl, jg, je
sub	jz, jc, jb, ja, jl, jg, je
inc	jz, jl, jg, je
dec	jz, jl, jg, je
test	jz, jc, jb, ja, jl, jg, js, jp, jo, je
and	jz, jc, jb, ja, jl, jg, js, jp, jo, je

Table 4: Fusible instruction pairs. The negated jumps, e.g., `jnz` for `jz`, are equally macro-fusible with the respective first instruction.

libraries for other architectures, such as Arm, from our analysis. Furthermore, we did not analyze libraries written in languages other than C/C++, resulting in 23 cryptographic libraries.

5.2 Static Analysis

Our evaluation is based on a static analysis of the libraries’ binaries. We disassembled the binaries and extracted all conditional jumps together with their preceding instructions, recording each instruction’s address and length. Next, we analyzed if the extracted instruction pairs can be macro-fused. At this stage, we did not yet consider the instruction placement, but only whether the two instructions are compatible. Therefore, we used the table of macro-fusible instructions from [11, Sec. 9.6] and extended it with an additional conditional jump: we found that the `je` conditional jump instruction can also be fused with preceding arithmetic, logic, and compare instructions. Table 4 provides an overview of fusible instruction pairs. Additionally, macro-op fusion is constrained by the type of operands of the first instruction. In Skylake-based microarchitectures, an instruction cannot be fused with a subsequent conditional jump: (i) if one of the operands uses `rip`-relative addressing, (ii) if the destination operand is a memory operand, or (iii) if the instruction has both an immediate and a memory source operand. Our static analysis accounts for this by removing instructions matching these criteria from the set of fusible instruction pairs.

Recall that macro-op fusion fails if the op and the jump of such a pair are in distinct L1I cache sets, i.e., the jump instruction starts at offset 64 (cf. Section 3.1). To analyze how many of the jumps fall into `noMFuse`, we analyzed all fusible operation-jump pairs and counted for how many of those the address of the conditional jump is 64B aligned.

On the other hand, macro-fusible instruction pairs are not cached and incur a delay in the instruction fetch unit if they span a 32B boundary but are not subject to `noMFuse` (cf. Section 3.2). Therefore, we analyzed whether the starting address of the first instruction was in a different 32B-aligned block than the last byte of the conditional jump.

Note that our analysis adopted a conservative approach by considering only the conditional jumps listed in Table 4 as candidates for macro-op fusion. While this selection aligns with prior work [11, 25], it is not exhaustive as it does not consider additional conditional jump instructions, such as `jae` or `jnge`. Given that these additional instructions are classified as conditional jumps,

this effectively reduces the fraction of `noMFuse` and `noμCache` reported in our analysis. Similarly, macro-op fusion does not allow for `rip`-relative memory accesses in the first instruction of a fusible instruction pair. While the `rip` register is permitted as an operand, our analysis excluded all instructions that access the `rip`. Due to the conservative nature of our approach, we anticipate a low rate of false positives.

5.3 Evaluation Results

Due to space limitations, we could not include the detailed results of all 666 libraries in this paper. Instead, Table 5 presents a representative summary of our findings. The complete list of libraries and our full evaluation results can be accessed at [26]. We summarize our findings below.

- Out of the 320 Ubuntu 24.04.2 libraries that we investigated, we identified 4,100,969 conditional jumps. From these jumps, 1.28% were subject to `noMFuse`, and 14.95% were caused by `noμCache`. Overall, the average proportion of `noMFuse` occurrences falls slightly below the expected value. In contrast, the proportion of `noμCache` occurrences remains above the lower bound of 10.93% (see Section 3.2) for 309 out of the 320 libraries, although our analysis uses a conservative heuristic. Notably, only a single library in our data set exhibited neither `noMFuse` nor `noμCache` jumps.
- In our analysis of 323 Windows 10 Pro 22H2 libraries, we identified a total of 18,769,762 conditional jumps, with 1.15% resulting from `noMFuse` and 13.69% from `noμCache`. Among the analyzed libraries, 42 libraries do not contain any `noMFuse` or `noμCache` jumps. Of these, 27 libraries contained no conditional jumps at all, while the remaining 15 may have leveraged the jump alignment optimization discussed in Section 6.1.
- Among the 23 cryptographic libraries we analyzed, we identified 396,093 conditional jumps. Among these jumps, 1.17% were caused by `noMFuse`, while 15.08% were attributed to `noμCache`. Consistent with the libraries in Ubuntu 24.04.2 and Windows 10 Pro 22H2, these results fall slightly below the expected value for `noMFuse`, and confirm our lower bound of 10.93% for `noμCache`.

Summary of results: Our empirical results validate our analysis in Section 3. Specifically, they confirm that conditional jumps are likely to exhibit abnormal execution timing in more than 15.1% (averaged over all occurrences of `noMFuse` and `noμCache` across all 666 libraries that we investigated). Notably, while the expected proportion of `noMFuse` occurrences is 1.56% (cf. Section 3.1), our empirical measurements show that only 1.17% of conditional jumps are affected by `noMFuse`. This discrepancy arises because our analysis in Section 3.1 conservatively assumes that all conditional jumps are macro-fusible. On the other hand, the measured proportion for `noμCache` occurrences is 13.93%, which aligns well with the expected range of 10.93 to 32.81% outlined in Section 3.2. In particular, this value closely matches the 14.06% measured in our sample in Section 3.2.

Table 5: Excerpt from our static analysis of 666 libraries across Ubuntu 24.04.2, Windows 10 Pro 22H2, and cryptographic libraries. For each library, we report the total number of conditional jumps and the proportion of jumps affected by noMFuse and no μ Cache.

Library	Conditional jumps	noMFuse	no μ Cache	Library	Conditional jumps	noMFuse	no μ Cache
Ubuntu 24.04.2							
libusb-1.0.so.0	1474	1.02%	16.76%	libkrb5.so.3	7564	1.20%	15.04%
libcurl-mb.so.8	363	1.65%	12.95%	libjbig.so.0	710	0.28%	11.13%
libthread_db.so	448	1.34%	15.18%	libidn2.so.0	447	1.79%	20.36%
libseccomp.so.2	1252	1.60%	18.13%	libhogweed.so.6	891	1.12%	14.48%
libquadmath.so.0	3553	1.07%	17.62%	libguestStoreClient.so.0	1884	0.96%	12.05%
libply-boot-client.so.5	135	3.70%	13.33%	libfreetype.so.6	15737	1.05%	15.85%
libpam.so.0	850	0.94%	16.47%	libestr.so.0	86	1.16%	9.30%
libncurses.so.6	2868	1.43%	15.17%	libdb-5.3.so	35937	1.17%	18.34%
libmpc.so.3	1425	1.12%	20.63%	libcap-ng.so.0	305	1.64%	18.36%
libm.so.6	7548	0.79%	10.73%	libc_malloc_debug.so	726	0.83%	13.36%
Windows 10 Pro 22H2							
wdag.dll	3316	1.09%	11.73%	vccorlib140.dll	4702	1.62%	16.55%
ink-rtscom.dll	2205	1.09%	11.75%	wns_push_client.dll	6929	0.92%	12.11%
msdac.dll	92	1.09%	8.70%	msedgeupdateres_da.dll	34	2.94%	0.00%
msdatl3.dll	3453	0.55%	5.50%	msedgeupdateres_mt.dll	33	3.03%	0.00%
hmmpapi.dll	353	2.27%	8.22%	libEGL.dll	8765	1.15%	13.83%
libEGL.dll	8175	1.57%	13.74%	msedge_elf.dll	55243	1.17%	13.95%
oneds.dll	61437	1.25%	15.29%	msvcp140.dll	8409	1.21%	12.74%
wns_push_client.dll	11618	1.29%	13.61%	wdag.dll	3316	1.09%	11.73%
mip_core.dll	44430	1.36%	14.50%	ie_to_edge_bho_64.dll	11162	1.33%	13.91%
concr140.dll	4024	1.24%	13.34%	EppManifest.dll	0	0.00%	0.00%
Cryptographic libraries							
libgcrypt 1.11.0	9568	1.09%	16.16%	tiny-AES-c 1.0.0	20	0.00%	10.00%
OpenSSL 3.4.0	63794	1.20%	16.71%	NSS 3.107	10564	1.12%	15.23%
LibreSSL 4.0.0	16730	1.16%	15.36%	libtomcrypt 1.18.2	7152	1.06%	15.86%
BoringSSL 0.20250114.0	31177	1.26%	16.00%	Nettle 3.10.1	2277	1.14%	13.92%
BearSSL 0.6	1636	1.47%	12.84%	MS SymCrypt 103.6.0	4681	2.16%	15.30%
Botan 3.6.1	72328	1.25%	16.07%	Intel IPP crypto 1.0.1	83515	1.01%	11.91%
Crypto++ 8.9	33829	1.07%	15.80%	NaCl 20110221	697	0.57%	12.20%
wolfSSL 5.7.6	10663	1.32%	15.82%	libsecp256k1 0.6.0	695	0.72%	16.12%
mbedtls 3.6.2	10157	1.19%	16.04%	libsodium 1.0.20	1871	1.50%	12.93%
Amazon s2n 1.5.11	9044	1.36%	17.80%	SPHINCS+	903	1.33%	17.17%
GnuTLS 3.7.11	23587	1.17%	14.27%	Monocypher 4.0.2	264	1.89%	11.74%
PQCrypto-SIDH 3.5.1	941	1.38%	14.56%				

6 Mitigation & Significance

In this section, we explore strategies to mitigate the alignment conditions responsible for noMFuse and no μ Cache, and quantify their impact across various real-world libraries.

6.1 Aligning Macro-Fusible Instructions

We now discuss strategies to mitigate the effects of noMFuse and no μ Cache on the affected microarchitectures. As discussed in Section 3.2, a prerequisite for no μ Cache is that the fusible instruction pair is not cached in the μ op cache, a consequence of the microcode update [16]. To compensate for the performance impact of this mitigation, one can rely on a software-based solution (as proposed by Intel in [16]). For example, the GNU Assembler introduced three new optimization flags, designed to align jump instructions to a 32-byte boundary by inserting segment prefixes or NOP instructions without altering code semantics. Among these

flags, `-malign-branch-boundary` defines the alignment boundary, `-malign-branch` specifies which instructions affected by the microcode update mitigation to align, and `-malign-branch-prefix` sets the maximum number of prefix bytes allowed for alignment. Additionally, the `-mbranches-within-32B-boundaries` configures default values for these three options, such that all conditional, unconditional, and fused jump instructions do not span a 32B boundary if this can be prevented with a maximum of five prefix bytes.

Note that this mitigation strategy successfully prevents *all* fusible instruction pairs from crossing the 32B boundary, thereby mitigating both noMFuse and no μ Cache. Given that this strategy prevents uncached macro-fusible instruction pairs, it naturally prevents no μ Cache but also mitigates noMFuse as a by-product. Specifically, noMFuse requires conditional jumps to be 64B-aligned. Preventing instruction pairs from spanning a 32B boundary indirectly disrupts this alignment, eliminating the conditions necessary for noMFuse.

6.2 Poor Visibility & Performance Impact

Although Intel has proposed a mitigation for `noμCache`, our analysis (cf. Table 5) reveals that *more than 600 of the libraries that we investigated in Windows 10 Pro 22H2 or Ubuntu 24.04.2 do not employ it to deter noMFuse and noμCache*. This confirms that Intel’s mitigation strategy is not easily accessible to practitioners. Moreover, documentation is sparse on this topic: GCC’s `-Wa, -mbranches-within-32B-boundaries` flag is neither listed in GCC’s option summary [13] nor mentioned in the GNU Assembler manual page [12].

To assess the effectiveness of this mitigation, we quantified its impact on both performance and code size across a range of cryptographic libraries. These libraries were selected because their source code and build configurations are publicly available, allowing controlled experimentation. We included only those libraries from Section 5.3 that offer built-in performance benchmarks, ensuring we measure metrics deemed relevant by their maintainers. Each benchmark was run five times with and without the mitigation, and we report average results. All experiments were executed on an isolated core of an Intel Xeon E-2286G CPU, which is based on the Coffee Lake microarchitecture, with 128GB RAM running Ubuntu 20.04 LTS. We then used the `size` command-line tool to assess changes in binary size due to the added padding.

The `-Wa, -mbranches-within-32B-boundaries` compiler flag implicitly sets default values for the `-malign-branch-boundary`, `-malign-branch`, and `-malign-branch-prefix` flags. Specifically:

- `-malign-branch-boundary` aligns branches to a 32-byte boundary, which is sufficient to mitigate both noMFuse and `noμCache` without the excessive padding that a 64-byte boundary would entail.
- `-malign-branch` determines which types of branches are aligned. By default, the compiler aligns conditional, fused, and unconditional jumps. We found that aligning only fused jumps—i.e., the jump type affected by the noMFuse- and `noμCache`-induced timing variability—is not supported by the compiler. Therefore, we experimented with configurations that either include or exclude unconditional jumps.
- `-malign-branch-prefix` sets the maximum number of prefix bytes (NOPs) that are used for alignment, limited to 5. We varied this value between 1 and 5 bytes, as a value of 0 effectively disables the mitigation.

While this mitigation enables fusion for noMFuse jumps and allows `noμCache` jumps to be cached in the `μop` cache, the subsequent cache set still needs to be accessed. We hypothesize that aligning loops to 32B or 64B boundaries may further improve performance by reducing the number of `μop` cache sets required to cache loops (which frequently execute jumps). Hence, we also experimented with loop alignment options. Note that for O2 and O3 optimization, the default loop alignment is 16 bytes.

Table 6 summarizes the results for selected configurations, while our full results are presented in Table 7. On average, Intel’s default mitigation yields a 1.4% speedup with a 1.11% code size overhead across 17 cryptographic libraries. Specifically, 14 libraries show measurable speedups over their default builds. A notable case is BearSSL, which achieves a 9.62% speedup at the cost of only a 1.72%

Table 6: Performance speedup for cryptographic libraries with the build-time mitigation. The code size overhead is reported in brackets for each library. Results are shown across various aligned jump types and prefix sizes, and reported relative (%) to the default build of the library. Negative values indicate slowdowns. The left column indicates results for the default configuration of the mitigation as suggested by Intel.

Branch	jcc+fused+jmp		jcc+fused
	5	3	
BearSSL	9.62 (1.72)	9.73 (1.72)	10.29 (1.60)
BoringSSL	0.83 (1.62)	0.78 (1.62)	0.34 (1.37)
Botan	1.31 (1.55)	0.31 (1.55)	1.74 (1.28)
Crypto++	0.15 (0.83)	0.18 (0.83)	0.08 (0.7)
GnuTLS	0.25 (0.91)	2.97 (0.91)	1.84 (0.71)
libgcrypt	0.04 (0.81)	0.03 (0.81)	0.1 (0.73)
LibreSSL	1.87 (1.60)	2.99 (1.60)	2.23 (1.04)
libsecp256k1	-0.13 (0.08)	0.19 (0.08)	0.07 (0.07)
libtomcrypt	3.33 (1.28)	3.3 (1.28)	2.83 (1.19)
mbedtls	0.84 (1.87)	0.85 (1.87)	0.37 (1.68)
Monocypher	0.38 (0.91)	0.28 (0.91)	0.14 (0.87)
MS SymCrypt	-0.33 (0.35)	-0.34 (0.35)	-0.5 (0.31)
Nettle	0.58 (1.0)	0.66 (1.0)	0.83 (0.82)
OpenSSL	2.28 (1.23)	2.01 (1.23)	2.18 (1.09)
PQCrypto	-0.32 (0.56)	0.05 (0.56)	-0.03 (0.52)
SPHINCS+	0.01 (0.61)	-0.02 (0.61)	0.0 (0.59)
WolfSSL	3.01 (1.96)	3.28 (1.99)	2.92 (1.75)

increase in binary size. In contrast, two libraries experience performance penalties of up to 0.33%, which we attribute to interference with other low-level optimizations caused by the added padding.

Our experiments (see Table 7) further show that loop alignment to 32 or 64 bytes does not consistently outperform Intel’s default configuration. Similarly, varying branch types and prefix sizes beyond the defaults does not reliably improve performance. However, two configurations stand out: Reducing the prefix size from 5 to 3 bytes (second column in Table 6) yields an average speedup of 1.6%, with no code size increase over the default mitigation. Furthermore, disabling alignment for unconditional jumps (last column in Table 6) increases the speedup by 0.1% while reducing the code size increase from 1.11% to 0.96%. Finally, when selecting the configuration that maximizes speedup for each library, we observe an average speedup of 2.15%—reaching up to 10.54%—with a negligible average code size increase of 0.01% over the default mitigation.

These findings suggest that there remains untapped performance potential, not only within cryptographic libraries but also across widely used system libraries, *resulting in large-scale energy efficiency across millions of devices*. In particular, wolfSSL—with more than two billion daily connections worldwide in 2022 [27]—and Amazon s2n-tls—used across numerous AWS services—updated their libraries following our recommendations [4, 28]. Within the Ubuntu 24.04.2 dataset, only a single library exhibited neither noMFuse nor `noμCache` jumps—implying that 97% of these libraries lack any mitigation against these slow-path cases and could benefit from adopting the proposed alignment strategy. Similarly, approximately 87% of the analyzed Windows 10 Pro 22H2 libraries could be further optimized by ensuring that macro-fusible instruction pairs do not cross 32-byte boundaries.

Table 7: Performance speedups for cryptographic libraries with build-time mitigations, and code size overheads in brackets. Results are shown across various aligned jump types, prefix sizes, and loop alignment boundaries, shown relative (%) to each library’s default build. Negative values indicate slowdowns. The grey column indicates Intel’s default mitigation, and the bolded value marks the maximum speedup for each library. Averages are shown in the last row.

Branch	jcc+fused+jmp						jcc+fused								
Prefix	5			4	3	2	1	16			5	4	3	2	1
Loop	16	32	64												
BearSSL	9.62 (1.72)	9.69 (1.72)	9.49 (1.72)	9.03 (1.72)	9.73 (1.72)	9.74 (1.72)	9.29 (1.72)	10.29 (1.60)	10.06 (1.60)	10.17 (1.60)	10.54 (1.60)	10.15 (1.60)			
BoringSSL	0.83 (1.62)	0.93 (2.31)	1.16 (3.41)	0.79 (1.62)	0.78 (1.62)	0.95 (1.62)	1.23 (1.62)	0.34 (1.37)	0.51 (1.37)	0.26 (1.37)	0.29 (1.37)	0.58 (1.37)			
Botan	1.31 (1.55)	1.27 (2.19)	-0.93 (3.37)	0.18 (1.55)	0.31 (1.55)	-1.34 (1.55)	-0.68 (1.55)	1.74 (1.28)	-0.06 (1.28)	0.16 (1.28)	0.61 (1.28)	-0.97 (1.28)			
Crypto++	0.15 (0.83)	0.16 (1.19)	0.16 (1.76)	0.11 (0.83)	0.18 (0.83)	0.11 (0.83)	0.1 (0.83)	0.08 (0.7)	0.06 (0.7)	0.02 (0.7)	-0.05 (0.7)	0.07 (0.7)			
GnuTLS	0.25 (0.91)	0.14 (0.91)	1.85 (0.91)	3.75 (0.91)	2.97 (0.91)	2.2 (0.91)	0.98 (0.9)	1.84 (0.71)	-0.09 (0.71)	-1.12 (0.71)	-0.96 (0.71)	-0.32 (0.71)			
libgcrypt	0.04 (0.81)	1.51 (1.42)	-0.01 (2.59)	0.06 (0.81)	0.03 (0.81)	0.04 (0.81)	0.01 (0.81)	0.1 (0.73)	0.04 (0.73)	0.09 (0.73)	0.06 (0.73)	0.04 (0.73)			
LibreSSL	1.87 (1.60)	1.15 (2.07)	0.62 (2.92)	2.04 (1.60)	2.99 (1.60)	4.18 (1.60)	2.39 (1.60)	2.23 (1.04)	1.92 (1.04)	1.53 (1.04)	1.14 (1.04)	1.09 (1.04)			
libsecp256k1	-0.13 (0.08)	-0.27 (0.13)	0.05 (0.21)	0.21 (0.08)	0.19 (0.08)	0.14 (0.08)	0.15 (0.08)	0.07 (0.07)	-0.04 (0.07)	-0.19 (0.07)	0.04 (0.07)	0.02 (0.07)			
libtomcrypt	3.33 (1.28)	2.42 (1.71)	2.63 (2.39)	3.06 (1.28)	3.3 (1.28)	2.93 (1.28)	2.72 (1.28)	2.83 (1.19)	2.94 (1.19)	3.43 (1.19)	2.95 (1.19)	2.36 (1.18)			
mbedtls	0.84 (1.87)	0.81 (2.46)	-2.2 (3.44)	0.76 (1.87)	0.85 (1.87)	-0.51 (1.88)	-0.65 (1.88)	0.37 (1.68)	0.49 (1.68)	0.4 (1.68)	-0.17 (1.68)	-0.61 (1.69)			
Monocypher	0.38 (0.91)	0.56 (1.45)	0.2 (2.06)	-0.04 (0.91)	0.28 (0.91)	2.46 (0.91)	1.65 (0.91)	0.14 (0.87)	0.0 (0.87)	0.15 (0.87)	0.77 (0.87)	0.54 (0.87)			
MS SymCrypt	-0.33 (0.35)	-0.33 (0.35)	-0.31 (0.35)	-1.04 (0.35)	-0.34 (0.35)	-0.24 (0.35)	-0.33 (0.35)	-0.5 (0.31)	-0.08 (0.31)	-0.87 (0.31)	-0.72 (0.31)	-1.28 (0.31)			
Nettle	0.58 (1.0)	0.78 (1.48)	0.8 (2.53)	0.61 (1.0)	0.66 (1.0)	0.61 (1.0)	0.51 (1.0)	0.83 (0.82)	0.84 (0.82)	0.73 (0.82)	0.8 (0.82)	0.66 (0.82)			
OpenSSL	2.28 (1.23)	1.43 (1.58)	1.23 (2.3)	1.92 (1.23)	2.01 (1.23)	1.69 (1.23)	1.73 (1.23)	2.18 (1.09)	2.39 (1.09)	2.55 (1.09)	1.83 (1.09)	1.95 (1.09)			
PQCrypto	-0.32 (0.56)	-0.07 (1.79)	0.12 (2.83)	-0.14 (0.56)	0.05 (0.56)	0.0 (0.56)	-0.09 (0.56)	-0.03 (0.52)	-0.1 (0.52)	0.14 (0.52)	0.07 (0.52)	0.01 (0.52)			
SPHINCS+	0.01 (0.61)	0.03 (1.01)	0.03 (1.68)	0.02 (0.61)	-0.02 (0.61)	0.0 (0.61)	-0.01 (0.61)	0.0 (0.59)	0.0 (0.59)	-0.02 (0.59)	-0.01 (0.59)	0.0 (0.59)			
WolfSSL	3.01 (1.96)	2.45 (3.03)	2.16 (4.95)	3.25 (1.99)	3.28 (1.99)	2.52 (1.99)	2.69 (1.99)	2.92 (1.75)	3.07 (1.75)	2.99 (1.75)	2.6 (1.75)	2.64 (1.75)			
average	1.40 (1.11)	1.33 (1.58)	1.00 (2.32)	1.45 (1.11)	1.60 (1.11)	1.50 (1.11)	1.28 (1.11)	1.50 (0.96)	1.29 (0.96)	1.20 (0.96)	1.16 (0.96)	1.00 (0.96)			

7 Covert Channels from Abnormal Conditional Jumps

So far, we have analyzed how misaligned conditional jump instructions impact execution time due to the specific behavior of the x86 front-end. Previous work has shown that such timing variations can be exploited by an adversary to leak sensitive data by constructing a side or covert channel [2, 10, 24]. We now quantify the extent to which these timing variations of misaligned conditional jump instructions can be exploited in a cross-core covert channel.

7.1 Setup

We consider the exemplary assembly code in Figure 9 that performs conditional branching based on secret data, where one branch contains an “abnormal” jump affected by noMFuse (line 23), while the other branch includes a “normal” jump (line 11). Based on our results in Section 3, such an alignment should occur with a probability of 15%.

Our example code iterates over 256 secret bits, branching based on their value. To eliminate timing discrepancies due to different instructions in the two branches, we execute identical computations in both branches. This is common practice to eliminate timing side-channels, e.g., when writing secure cryptographic software. The sub and the conditional jump should be macro-fused unless the jump is aligned to a 64-byte boundary—this is the case for the jump in line 23—thereby adding a noticeable delay to the computation. As demonstrated in Section 3, this alignment introduces measurable execution delays, enabling an adversary to infer secret-dependent timing variations. We run this code on an Intel Xeon E-2176G CPU, operating at 4 GHz clock frequency, with 128GB RAM running Ubuntu 20.04 LTS.

7.2 Covert-Channel

We assume a sender who is running the code in Figure 9, while the receiver operates on a different physical core within the same machine. Moreover, we consider an example in which the sender

and receiver synchronize both at the beginning and at the end of the code snippet shown in Figure 9 using Intel’s Transactional Synchronization Extensions (TSX). In line with prior work [7], the receiver gets the abort signal immediately when the target code starts and ends, and uses these signals for measuring the execution time. Note that our covert channel does not depend on the availability of TSX, as synchronization can also be achieved through alternative mechanisms, including page faults [19], cache contention [8, 15, 19] or atomic operations on shared variables [6], as well as benign messages when permitted by the application [2]. These mechanisms can be used to signal the receiver when to start and stop execution-time measurements.

Our results are summarized in Figure 10. We measure the error rates incurred by the different channel capacities. More specifically, we encode the number of bits to be transmitted using the Hamming weight of the local variable accessed in line 17. For example, we can effectively send 1 bit from the sender to the receiver by setting the local variable in line 17 to have a Hamming weight of either 0 or 256. Similarly, the sender can encode up to 2 bits by setting the local variable to have a Hamming weight of 0 (transmitting bits “00”), 83 (transmitting bits “01”), 166 (transmitting bits “10”), and 256 (transmitting bits “11”), respectively (ensuring maximum spread of the Hamming weight of the local variable, hence maximizing the ability of the receiver to decode the message correctly). Notice that with a local variable size of 256 bits, the sender can encode at most 8 bits at a time on the channel; it is straightforward to see here that selecting a larger variable size allows the sender to encode additional bits per transmission.

Our results suggest that one can leverage our covert-channel to encode up to 5 bits in approximately 1238.73 cycles with an accuracy as high as 95.46%. In other words, we can achieve a maximum throughput of up to 16.14 Mbps (it takes on average 0.310 μ s for the loop in Figure 9 to complete in our setup) with an error rate of 4.54%. In comparison, note that the maximum throughput achieved with the covert-channel in [25] is 858 kbps with a 5.85% error

Table 8: List of hardware performance counters (HPCs) on Intel CPUs and the specific events they capture.

HPC	Description
FRONTEND_RETIRE.DSB_MISS	Number of retired instructions that experienced a μ op cache miss.
IDQ_UOPS_NOT_DELIVERED.CYCLES_0_DELIV_CORE	Number of cycles the IDQ did not deliver any μ ops to the back-end without back-end stalls.
UOPS_ISSUED_STALL_CYCLES	Number of cycles the RAT did not issue any μ ops to the RS.
UOPS_ISSUED_ALL	Number of μ ops the RAT issued to the RS.
INSTRUCTIONS	Number of instructions.
BACLEAR.S.ANY	Number of front-end resteers due to a BPU misprediction.

```

1 131a: lfence
2 131d: rdtsc
3 131f: mov    rdi,rax
4 1322: lfence
5 1325: mov    eax,0xff
6 132a: mov    esi,0x1
7 132f: mov    r9d,0x1
8 1335: jmp    1340 <main+0x160>
9 1337: imul   r9,r12
10 133b: sub    eax,0x1
11 133e: jb    1362 <main+0x182>
12 1340: mov    edx,eax
13 1342: mov    ecx,eax
14 1344: sar    edx,0x6
15 1347: not    ecx
16 1349: movsxd rdx,edx
17 134c: mov    rdx,QWORD PTR [rsp+rdx*8+0x10]
18 1351: shl    rdx,c1
19 1354: test   rdx,rdx
20 1357: jns    1337 <main+0x157>
21 1359: imul   rsi,r12
22 135d: sub    eax,0x1
23 1360: jae    1340 <main+0x160>
24 1362: lfence
25 1365: rdtsc

```

Figure 9: Example of a loop that transmits information depending on branch location. The “fast” branch is highlighted in blue, and the “slow” branch in red.

rate. Similarly, the covert-channel of [10] achieves a maximum throughput of 1.41 Mbps with 0% error rate, and the one in [24] achieves a throughput of 966 kbps with an error rate of 0.22%.

8 Conclusion

In this paper, we measured and analyzed the timing variations of conditional jump instructions caused by their placement in a binary. Specifically, we demonstrate that the position of a conditional jump instruction affects macro-op fusion and the caching of the corresponding μ op in the μ op cache, which in turn influences instruction fetch time. Through extensive measurements, we assessed the prevalence of this timing variability and found that up to 15.6% of all conditional jumps incur additional execution cycles. We validate our analysis through a large-scale study of over 600 libraries in Windows 10 Pro 22H2 and Ubuntu 24.04.2, along with several widely used cryptographic libraries. Our results are striking: only one out of 320 Ubuntu libraries exhibited neither noMFuse nor no μ Cache jumps; only 42 out of 323 Windows Pro libraries were free of jumps subject to noMFuse or no μ Cache; and 0 of the 23 cryptographic libraries were not affected by noMFuse or no μ Cache. We quantified the impact of this observation based on the cryptographic libraries, showing an average speedup of 2.15% and up to 10.54% speedup when using the suggested mitigation.

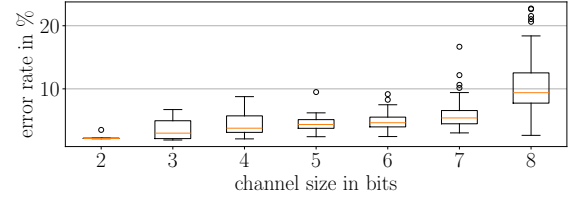


Figure 10: Error rates for different channel capacities based on our covert-channel. Here, every data point is averaged over 100 independent runs.

Moreover, we show that these timing variabilities enable the creation of a practical covert channel, resulting in a throughput of up to 16.14 Mbps. We therefore urge developers and practitioners to ensure that macro-fusible instructions are 32-byte aligned in their code. To ensure full reproducibility of our results, all associated source code and obtained measurements are available open-source at [26].

Acknowledgments

This work is partly funded by the Deutsche Forschungsgemeinschaft (DFG, German Research Foundation) under Germany’s Excellence Strategy - EXC 2092 CASA - 390781972, and the European Union’s Horizon 2020 research and innovation program (REWIRE, Grant Agreement No. 101070627, and ACROSS, Grant Agreement No. 101097122). Views and opinions expressed are, however, those of the authors only and do not necessarily reflect those of the European Union. Neither the European Union nor the granting authority can be held responsible for them.

References

- [1] Onur Aciicmez, Cetin Kaya Koç, and Jean-Pierre Seifert. 2007. Predicting Secret Keys Via Branch Prediction. In *Topics in Cryptology - CT-RSA 2007, The Cryptographers’ Track at the RSA Conference 2007, San Francisco, CA, USA, February 5-9, 2007, Proceedings (Lecture Notes in Computer Science, Vol. 4377)*, Masayuki Abe (Ed.). Springer, 225–242. doi:10.1007/11967668_15 DBLP:conf/cryptoe/AciicmezKS07.
- [2] Alejandro Cabrera Aldaya, Billy Bob Brumley, Sohaib ul Hassan, Cesar Pereida Garcia, and Nicola Tuveri. 2019. Port Contention for Fun and Profit. In *2019 IEEE Symposium on Security and Privacy, SP 2019, San Francisco, CA, USA, May 19-23, 2019*. IEEE, 870–887. doi:10.1109/SP.2019.00066 DBLP:conf/sp/AldayaBHGT19.
- [3] José Bacelar Almeida, Manuel Barbosa, Gilles Barthe, François Dupressoir, and Michael Emmi. 2016. Verifying Constant-Time Implementations. In *25th USENIX Security Symposium, USENIX Security 16, Austin, TX, USA, August 10-12, 2016*, Thorsten Holz and Stefan Savage (Eds.). USENIX Association, 53–70. https://www.usenix.org/conference/usenixsecurity16/technical-sessions/presentation/almeida DBLP:conf/uss/AlmeidaBBDE16.
- [4] Amazon Web Services (AWS). 2025. s2n-tls Release v1.5.18. https://github.com/aws/s2n-tls/releases/tag/v1.5.18. Accessed: 2025-12-15.

[5] Marc Andryesco, David Kohlbrenner, Keaton Mowery, Ranjit Jhala, Sorin Lerner, and Hovav Shacham. 2015. On Subnormal Floating Point and Abnormal Timing. In *2015 IEEE Symposium on Security and Privacy, SP 2015, San Jose, CA, USA, May 17-21, 2015*. IEEE Computer Society, 623–639. doi:10.1109/SP.2015.44 DBLP:conf/sp/AndryescoKMJLS15.

[6] Atri Bhattacharyya, Alexandra Sandulescu, Matthias Neugschwandner, Alessandro Sorniotti, Babak Falsafi, Matthias Payer, and Anil Kurmus. 2019. SMoTherSpectre: Exploiting Speculative Execution through Port Contention. In *Proceedings of the 2019 ACM SIGSAC Conference on Computer and Communications Security, CCS 2019, London, UK, November 11-15, 2019*, Lorenzo Cavallaro, Johannes Kinder, XiaoFeng Wang, and Jonathan Katz (Eds.). ACM, 785–800. doi:10.1145/3319535.3363194

[7] Samira Briongos, Ida Bruhns, Pedro Malagón, Thomas Eisenbarth, and José Manuel Moya. 2021. Aim, Wait, Shoot: How the CacheSniper Technique Improves Unprivileged Cache Attacks. In *IEEE European Symposium on Security and Privacy, EuroS&P 2021, Vienna, Austria, September 6-10, 2021*. IEEE, 683–700. doi:10.1109/EUROSP51992.2021.00051

[8] Jo Van Bulck, Marina Minkin, Ofir Weisse, Daniel Genkin, Baris Kasikci, Frank Piessens, Mark Silberstein, Thomas F. Wenisch, Yuval Yarom, and Raoul Strackx. 2018. Foreshadow: Extracting the Keys to the Intel SGX Kingdom with Transient Out-of-Order Execution. In *27th USENIX Security Symposium, USENIX Security 2018, Baltimore, MD, USA, August 15-17, 2018*, William Enck and Adrienne Porter Felt (Eds.). USENIX Association, 991–1008. https://www.usenix.org/conference/usenixsecurity18/presentation/bulck DBLP:conf/uss/BulckMWGKPSWYS18.

[9] Claudio Canella, Daniel Genkin, Lukas Giner, Daniel Gruss, Moritz Lipp, Marina Minkin, Daniel Moghimi, Frank Piessens, Michael Schwarz, Berk Sunar, Jo Van Bulck, and Yuval Yarom. 2019. Fallout: Leaking Data on Meltdown-resistant CPUs. In *Proceedings of the 2019 ACM SIGSAC Conference on Computer and Communications Security, CCS 2019, London, UK, November 11-15, 2019*, Lorenzo Cavallaro, Johannes Kinder, XiaoFeng Wang, and Jonathan Katz (Eds.). ACM, 769–784. doi:10.1145/3319535.3363219 DBLP:conf/ccs/CanellaGGLMMP019.

[10] Shuwen Deng, Bowen Huang, and Jakub Szefer. 2022. Leaky Frontends: Security Vulnerabilities in Processor Frontends. In *IEEE International Symposium on High-Performance Computer Architecture, HPCA 2022, Seoul, South Korea, April 2-6, 2022*. IEEE, 53–66. doi:10.1109/HPCA53966.2022.00013 DBLP:conf/hpca/DengHS22.

[11] Agner Fog. 2024. The microarchitecture of Intel, AMD, and VIA CPUs. <https://www.agner.org/optimize/microarchitecture.pdf>. [Online; accessed 2024-08-28].

[12] Inc. Free Software Foundation. 2025. *as(1) - Linux man page*. <https://linux.die.net/man/1/as> [Online; accessed 09.03.2025].

[13] Inc. Free Software Foundation. 2025. *GCC Option Summary*. <https://gcc.gnu.org/onlinedocs/gcc/Option-Summary.html> [Online; accessed 9 March 2025].

[14] Johann Großschädl, Elisabeth Oswald, Dan Page, and Michael Tunstall. 2009. Side-Channel Analysis of Cryptographic Software via Early-Terminating Multiplications. In *Information, Security and Cryptology - ICISC 2009, 12th International Conference, Seoul, Korea, December 2-4, 2009, Revised Selected Papers (Lecture Notes in Computer Science, Vol. 5984)*, Dong Hoon Lee and Seokhie Hong (Eds.). Springer, 176–192. doi:10.1007/978-3-642-14423-3_13 DBLP:conf/icisc/GrossschadlOPT09.

[15] Casen Hunger, Mikhail Kazdagli, Ankit Singh Rawat, Alexandros G. Dimakis, Sriram Vishwanath, and Mohit Tiwari. 2015. Understanding contention-based channels and using them for defense. In *21st IEEE International Symposium on High Performance Computer Architecture, HPCA 2015, Burlingame, CA, USA, February 7-11, 2015*. IEEE Computer Society, 639–650. doi:10.1109/HPCA.2015.7056069

[16] Intel. 2019. *Mitigations for Jump Conditional Code Erratum*. <https://www.intel.com/content/www/us/en/content-details/841076/intel-mitigations-for-jump-conditional-code-erratum.html> Revision 1.0.

[17] Intel. 2024. Optimizing Earlier Generations of Intel 64 and IA-32 Processor Architectures, Throughput, and Latency. <https://www.intel.com/content/www/us/en/content-details/821614/optimizing-earlier-generations-of-intel-64-and-ia-32-processor-architectures-throughput-and-latency.html>. Version 050.

[18] Jan Jancar, Marcel Fourné, Daniel De Almeida Braga, Mohamed Sabt, Peter Schwabe, Gilles Barthe, Pierre-Alain Fouque, and Yasemin Acar. 2024. They're not that hard to mitigate: What Cryptographic Library Developers Think About Timing Attacks. In *Software Engineering 2024, Fachtagung des GI-Fachbereichs Softwaretechnik, Linz, Austria, February 26 - March 1, 2024 (LNI, Vol. P-343)*, Rick Rabiser, Manuel Wimmer, Iris Groher, Andreas Wortmann, and Bianca Wiesmayr (Eds.). Gesellschaft für Informatik e.V., 143–144. doi:10.18420/SW2024_47 DBLP:conf/se/JancarFBSSBFA24.

[19] Jianyu Jiang, Claudio Soriente, and Ghassan Karame. 2022. On the Challenges of Detecting Side-Channel Attacks in SGX. In *25th International Symposium on Research in Attacks, Intrusions and Defenses, RAID 2022, Limassol, Cyprus, October 26-28, 2022*. ACM, 86–98. doi:10.1145/3545948.3545972

[20] Joonsung Kim, Hamin Jang, Hunjun Lee, Seungho Lee, and Jangwoo Kim. 2021. UC-Check: Characterizing Micro-operation Caches in x86 Processors and Implications in Security and Performance. In *MICRO '21: 54th Annual IEEE/ACM International Symposium on Microarchitecture, Virtual Event, Greece, October 18-22, 2021*. ACM, 550–564. doi:10.1145/3466752.3480079 DBLP:conf/micro/KimJJKL21.

[21] Paul Kocher, Jann Horn, Anders Fogh, Daniel Genkin, Daniel Gruss, Werner Haas, Mike Hamburg, Moritz Lipp, Stefan Mangard, Thomas Prescher, Michael Schwarz, and Yuval Yarom. 2019. Spectre Attacks: Exploiting Speculative Execution. In *2019 IEEE Symposium on Security and Privacy, SP 2019, San Francisco, CA, USA, May 19-23, 2019*. IEEE, 1–19. doi:10.1109/SP.2019.00002 DBLP:conf/sp/KocherHFGGHLM19.

[22] LWN.net. 2017. Intel Skylake/Kaby Lake processors: broken hyper-threading. <https://lwn.net/Articles/726496/>. [Online; accessed 2025-07-22].

[23] Antoon Purnal, Furkan Turan, and Ingrid Verbauwheide. 2021. Prime+Scope: Overcoming the Observer Effect for High-Precision Cache Contention Attacks. In *CCS '21: 2021 ACM SIGSAC Conference on Computer and Communications Security, Virtual Event, Republic of Korea, November 15 - 19, 2021*, Yongdae Kim, Jong Kim, Giovanni Vigna, and Elaine Shi (Eds.). ACM, 2906–2920. doi:10.1145/3460120.3484816 DBLP:conf/ccs/PurnalTV21.

[24] Xida Ren, Logan Moody, Mohammadkazem Taram, Matthew Jordan, Dean M. Tullsen, and Ashish Venkat. 2021. I See Dead *oops*: Leaking Secrets via Intel/AMD Micro-Op Caches. In *48th ACM/IEEE Annual International Symposium on Computer Architecture, ISCA 2021, Virtual Event / Valencia, Spain, June 14-18, 2021*. IEEE, 361–374. doi:10.1109/ISCA52021.2021.00036 DBLP:conf/isca/RenMTJTV21.

[25] Han Wang and Ming Tang. 2023. Cross-Core and Robust Covert Channel Based on Macro-Op Fusion. *Security and Communication Networks* 2023, 1 (2023), 8031859. doi:10.1155/2023/8031859

[26] Annika Wilde, Samira Briongos, Claudio Soriente, and Ghassan Karame. 2026. *Artifact On Abnormal Execution Timing of Conditional Jump Instructions: Repository on GitHub*. https://github.com/RUB-InfSec/abnormal_conditional_jump_timing

[27] wolfSSL. 2022. wolfSSL 2022 Annual Report. <https://www.wolfssl.com/wolfssl-2022-annual-report/>. Accessed: 2025-12-15.

[28] wolfSSL. 2025. WolfSSL Commit 151b9f0. <https://github.com/wolfSSL/wolfssl/commit/151b9f0e74f4e635e9360ca3e61c502de49b9bfc>. Accessed: 2025-12-15.

[29] Yuval Yarom and Katrina Falkner. 2014. FLUSH+RELOAD: A High Resolution, Low Noise, L3 Cache Side-Channel Attack. In *Proceedings of the 23rd USENIX Security Symposium, San Diego, CA, USA, August 20-22, 2014*, Kevin Fu and Jaeyeon Jung (Eds.). USENIX Association, 719–732. <https://www.usenix.org/conference/usenixsecurity14/technical-sessions/presentation/yarom> DBLP:conf/uss/YaromF14.